Article

Not peer-reviewed version

Power Production and Blade Fatigue of a Wind-Turbine Array Subjected to Active Yaw Control

Mou Lin and Fernando Porté-Agel *

Posted Date: 24 January 2023

doi: 10.20944/preprints202301.0417.v1

Keywords: wind power; wind turbine fatigue; active yaw control

Article

Power Production and Blade Fatigue of a Wind-Turbine Array Subjected to Active Yaw Control

Mou Lin and Fernando Porté-Agel *

Wind Engineering and Renewable Energy Laboratory (WiRE), École Polytechnique Fédérale de Lausanne (EPFL), EPFL-ENAC-IIE-WIRE, Lausanne 1015, Switzerland.
* Correspondence: fernando.porte-agel@epfl.ch

Abstract: This study investigates the power production and blade fatigue of a three-turbine array subjected to active yaw control (AYC) in full-wake and partial-wake configurations. A framework of two-way coupled large-eddy simulation (LES) and aeroelastic blade simulation is applied to simulate the atmospheric boundary-layer (ABL) flow through the turbine array and the structural responses of the turbine blades. Mean power outputs and blade fatigue loads are extracted from the simulation results. By exploring the feasible AYC decision space, we find that (a) in the full-wake configuration, the local power-optimal AYC strategy with positive yaw angles endures less flapwise blade fatigue and more edgewise blade fatigue than the global power-optimal strategy; (b) in the partial-wake configuration, applying positive AYC in certain inflow wind directions achieves higher optimal power gains than that in the full-wake scenario and reduces the blade fatigue from the non-yawed benchmark. Through a theoretical analysis based on the blade element momentum theory, we reveal that the aforementioned differences in flapwise blade fatigue between the positively and negatively yawed turbine are due to the differences in the azimuthal distributions of the local relative velocity on blade sections, resulting from the combined effects of vertical wind shear and blade rotation. Furthermore, the difference in the blade force between the positively and negatively yawed front-row turbine induces different wake velocity and turbulence distributions, causing different fatigue loads on the downwind turbine exposed to the wake.

Keywords: wind power; wind turbine fatigue; active yaw control

---

1. Introduction

Active yaw control (AYC) is a wind farm control strategy that has recently attracted wide interest in the wind energy community. When wind farm operators apply AYC, they intentionally yaw upwind turbines to steer their wakes away from downwind turbines. While the yawed turbines reduce their power outputs, with a proper AYC strategy, the wind farm can yield more power and endure less structural fatigue because wake interference between wind turbines is mitigated.

Several experimental [1–6] and computational [7–12] studies have been conducted to investigate the effectiveness of AYC for wind farm power optimisation. Recently, there has been growing interest among wind energy researchers in jointly considering fatigue reduction and power optimisation when applying AYC. Kragh and Hansen [13] first pointed out the potential of AYC for reducing load variations on wind turbine blades caused by vertical wind shear. Zalkind and Pao [14] later investigated the fatigue loads of a stand-alone wind turbine at different yaw angles. They found that for a clockwise-rotating (when viewed from the front) wind turbine in vertically sheared wind, positive yaw strategies (counter-clockwise yaw when viewed from the top) decrease the damage equivalent load (DEL) of the out-of-plane (OOP) blade bending moment, while negative yaw strategies increase it. Using large-eddy simulation (LES), Fleming et al. [15] studied a two-turbine case subjected to AYC in the full-wake condition, and they reported that applying proper positive yaw strategies can increase power outputs and reduce turbine fatigue. Damiani et al. [16] measured the component loads acting on a utility-scale turbine under yaw conditions and also confirmed the dichotomy of positive yaw and negative yaw in wind turbine loads.

With the studies mentioned above confirming the potential of AYC for achieving power gain and fatigue reduction, wind energy researchers have conducted several optimisation studies that applied AYC to wind farms. Gebraad et al. [17] optimised the annual power production of a hypothetical wind farm with AYC using a parametric wake model. Dijk et al. [18] further incorporated a simplified load model into the wake model used in [17] and performed a multi-objective optimisation of the power production and fatigue loads of a hypothetical wind farm subjected to AYC. Using a reduced-order flow solver, Kanev et al. [19] applied AYC to real-world wind farms to optimise the lifetime power production and fatigue loading. Reyes et al. [20] developed a computationally cheap look-up table approach to optimise fatigue loads in wind farms and validated it with wind tunnel and full-scale field tests. Lin and Porté-Agel [21] used LES to investigate Pareto-optimal AYC strategies for an array of three miniature wind turbines to maximise power production and minimise fatigue loads. They found that Pareto-optimal yaw strategies with gradually decreasing yaw angles from upwind to downwind turbines.

As shown in the literature, AYC can potentially increase the power outputs and mitigate the fatigue loads of a wind farm with proper yaw strategies. However, a poorly chosen yaw strategy can also significantly increase wind turbine fatigue loads while only achieving marginal power gains. Therefore, the main objective of this study is to understand how the application of different AYC strategies affects the power production and fatigue loading for a wind farm under various inflow configurations.

The rest of the paper is structured as follows: in Section 2, we discuss the two-way coupled aeroelastic LES frameworks used in this study and the methodology for evaluating power production and fatigue loads; in Section 3, we present the results of the simulations using different configurations; in Section 4, we present a theoretical analysis on the differences in flapwise blade fatigue in the turbines under positive and negative yaw strategies; in Section 5, we present the conclusions drawn from these findings and discuss possible extensions of this study.

2. Methodology

2.1. Governing equations

This study uses the GPU-accelerated version of the in-house WiRE-LES code [12,22–24], which solves the spatially-filtered, incompressible Navier-Stokes equations:

$$\frac{\partial \widetilde{u}_i}{\partial x_i} = 0, \tag{1}$$

$$\frac{\partial \widetilde{u}_i}{\partial t} + \widetilde{u}_j \left(\frac{\partial \widetilde{u}_i}{\partial x_j} - \frac{\partial \widetilde{u}_j}{\partial x_i} \right) = -\frac{\partial \widetilde{p}^*}{\partial x_i} - \frac{\partial \tau_{ij}}{\partial x_j} + \frac{F_p}{\rho}\delta_{i1} - \frac{\widetilde{f}_i}{\rho}, \tag{2}$$

where the subscript i represents the streamwise ($i = 1$), spanwise ($i = 2$) and vertical ($i = 3$) directions of the ground-fixed coordinate system x - y - z 1), respectively, $\widetilde{u}_i$ is the spatially filtered flow velocity, $\widetilde{p}^*$ is the modified kinematic pressure, F_p is the pressure gradient imposed to the flow, $\tau_{ij} = \widetilde{u_i u_j} - \widetilde{u}_i \widetilde{u}_j$ is the kinematic sub-grid scale stress, and $\widetilde{f}_i$ represents the forces exerted by the wind turbine blades, the nacelle, and the tower on the flow.

To incorporate aeroelasticity in the simulation, we treat the rotating wind turbine blades as 1D Euler-Bernoulli beams governed by the dynamic Euler-Bernoulli equations [25]:

$$\frac{\partial^2 q_k}{\partial t^2} + \frac{1}{\mu}\frac{\partial^2 M_k}{\partial r^2} = \frac{1}{\mu}\frac{\partial}{\partial r}\left(\int_r^R \mu \omega^2 r dr \frac{\partial q_k}{\partial r}\right) + g_k + \frac{\hat{f}_k}{\mu}, \tag{3}$$

$$M_k = K_{kl}\frac{\partial^2 q_l}{\partial r^2}, \tag{4}$$

where the subscript k specifies the flapwise ($k = 1$) and edgewise ($k = 2$) directions of the blade-following coordinate system x'_n - y'_n - z'_n for the nth blade (Figure 1), r is the distance between the blade element and the hub centre, q_k is the blade deformation, M_k is the blade bending moment, g_k is the component of gravitational acceleration in the kth direction, μ is the blade mass per unit length, $\hat{f}_k$ is the aerodynamic load exerted by the flow on the blade, K_{kl} is the stiffness matrix of the blade section, and ω is the rotational speed of the rotor.

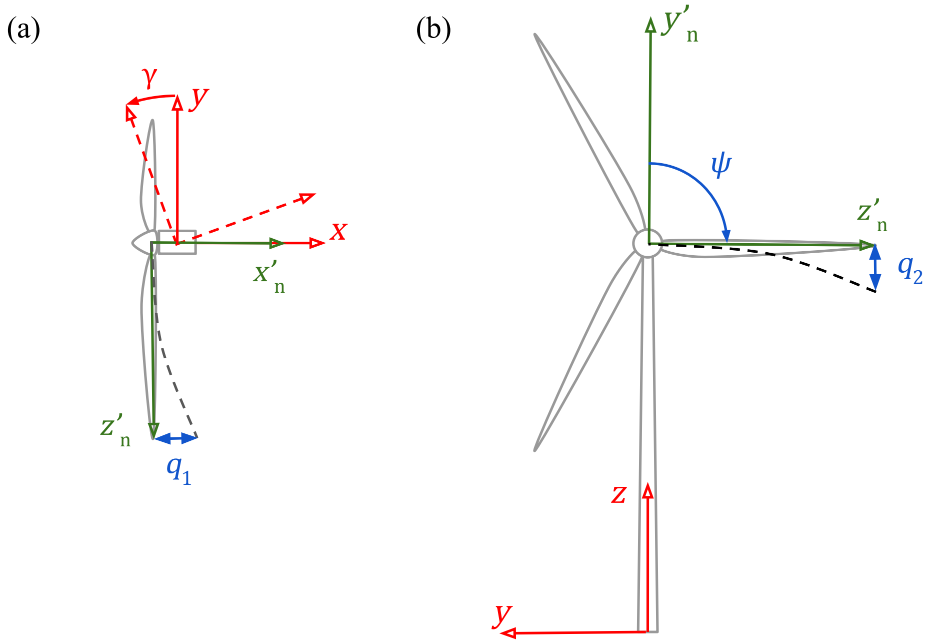

Figure 1. The ground-fixed coordinate system x - y - z for solving the filtered Navier-Stokes equations and the blade-following coordinate system x'_n - y'_n - z'_n for solving the Euler-Bernoulli beam equations for the nth blade: (**a**) top view; (**b**) front view. ψ is the phase angle of the blade. γ is the yaw angle of the turbine. The positive directions of ψ and γ follow the right-hand rule.

2.2. Simulation setup

In the WiRE-LES code, the filtered Navier-Stokes equations are solved numerically using the pseudo-spectral method in the horizontal directions (x and y) and the second-order finite-difference scheme in the vertical direction z. Time integration is done using the second-order Adam-Bashforth method. The sub-grid scale stress term is parametrised by the modulated gradient model [26]. The body forces induced by the wind-turbine blades are parametrised by the elastic actuator line model (EALM) proposed by Meng et al. [25]. The EALM simultaneously resolves the aerodynamic forces on turbine blade elements as the classical ALM [27] and solves the discretised Euler-Bernoulli beam equations using the finite-difference time-domain method to obtain blade deformations. The deformations are then used to update the ALM calculation in the next time step. The two-way coupling procedure in the EALM is summarised in Figure 2.

In this study, the simulation domain ($L_x \times L_y \times L_z$ = 4096 m × 2048 m × 1024 m), shown in Figure 3, is discretised into a 512 × 256 × 512 grid uniformly in each direction. A wind-turbine array consisting of three NREL 5 MW reference wind turbines [28], with a 7D distance between each turbine, is placed in the simulation domain. The wind turbines are not tilted. The first two wind turbines are subjected to yaw control, while the last turbine is not yawed. In the vertical direction (z) of the domain, a slip-wall boundary condition is applied to the top, and a non-penetration wall boundary condition with specified stresses according to the logarithmic law of the wall is applied to the bottom. Periodic boundary conditions are applied to the lateral boundaries in the horizontal directions. The inflow is generated by a precursor simulation without the wind turbine array and is then imposed at the

doi:10.20944/preprints202301.0417.v1

inlet section of the simulation domain with wind turbines. A buffer section is added in front of the inflow section to transform the flow from the outlet to the inlet of the simulation domain through a smooth weighting function. The mean streamwise hub-height inflow velocity $\overline{u}_{in} = 10$ m/s, and the streamwise hub-height inflow turbulence $I_u = 7.5\%$.

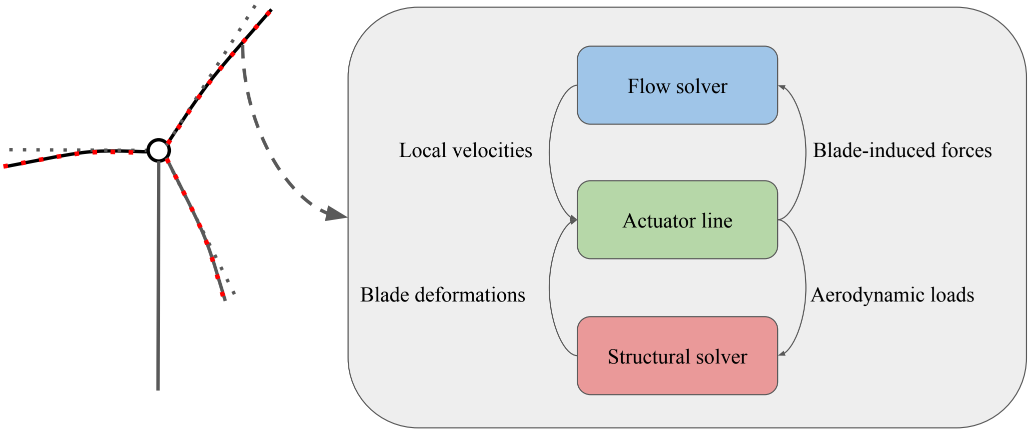

Figure 2. The coupling procedure between the flow solver and the structural solver in the EALM. The arrows in the flowchart represent the variable passing between different modules of the solver.

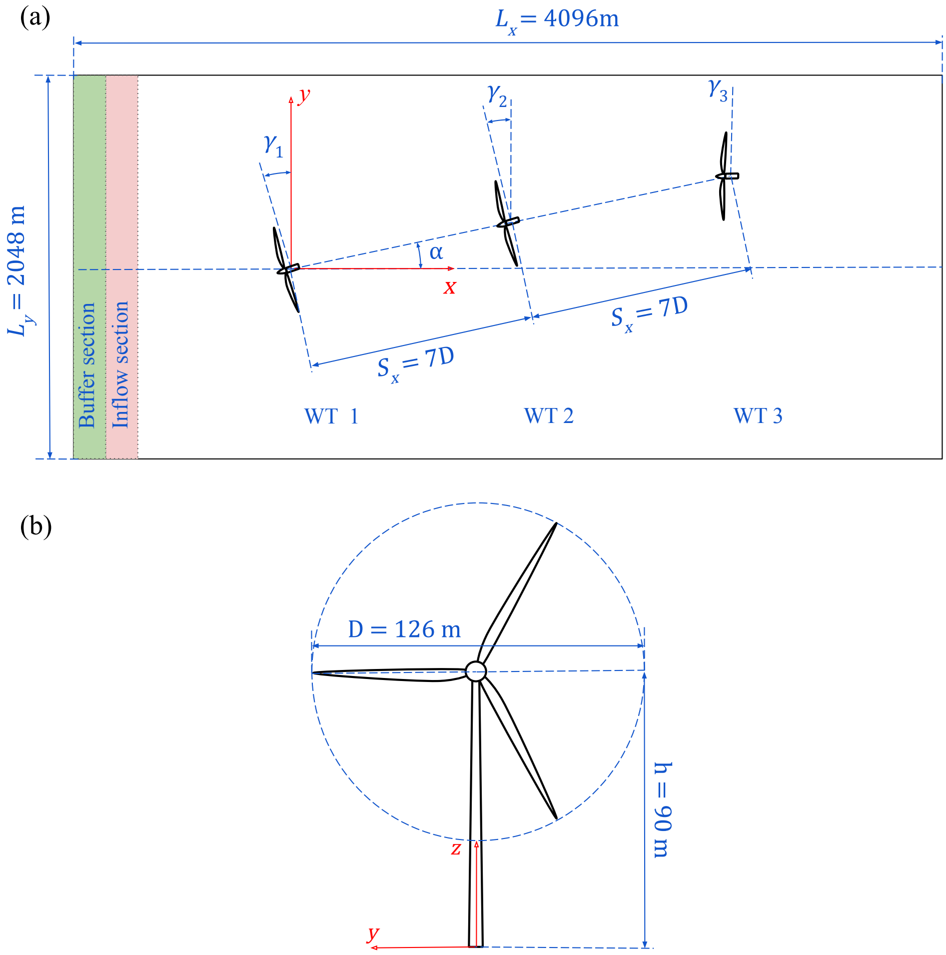

Figure 3. Schematic plots (not to scale) of (**a**) the simulation domain; (**b**) NREL 5MW reference wind turbine.

doi:10.20944/preprints202301.0417.v1

2.3. Fatigue evaluation

In this study, wind turbine fatigue damage is quantified by the damage equivalent loads (DELs) of blade-root bending moments (flapwise and edgewise). The procedures for computing DELs are listed as follows [29]:

- Extract time series of blade-root bending moments from the LES coupled with the EALM.
- Apply the rainflow cycle-counting algorithm and extract the histograms of load-cycle means M_{mean} and load-cycle ranges M_{range}.
- Use Goodman's rule to correct the effect of mean loads on fatigue damages and obtain the corrected cycle range $M'_{range,k}$ for the kth bin of the histogram:

  $$M'_{range,k} = \frac{M_{range,k}}{1 - \frac{M_{mean,k}}{\sigma M_{max}}}, \tag{5}$$

  where M_{max} is the maximum bending moment of the time series, σ is a safety factor, and its value is chosen as 1.5 [30].
- Use the Palmgren-Miner rule, which assumes linear accumulation of fatigue damages, to compute DELs:

  $$M_{DEL} = \left(\frac{\sum_{k=1}^{n_b} n_k M'^{\,m}_{range,k}}{N_{ref}} \right)^{1/m}, \tag{6}$$

  where n_b is the total bin number of the histogram extracted from the rainflow cycle-counting, n_k is the cycle count of the kth bin of the histogram, N_{ref} is the reference cycle number, and m is a material parameter which takes the value of 10 for composite materials.

3. Simulation Results

In this section, we present the simulation results of different AYC strategies in full-wake and partial-wake configurations. The AYC decision space is spanned by the yaw angles of the first two turbines in the array (WT 1 and WT 2): $\mathbf{\Gamma} = \{\gamma_1 : -30°, -25°, ..., 25°, 30°\} \times \{\gamma_2 : -30°, -25°, ..., 25°, 30°\}$, and the yaw angle of the last turbine is fixed to $0°$. A time window of 800 s is chosen to extract the mean velocity fields, mean power outputs and fatigue loads based on the recommendations of IEC standards [30].

3.1. Velocity deficits

Figure 4 shows the contours of normalised mean streamwise velocity deficits $\Delta\overline{u}/\overline{u}_{in}$ of six representative cases (Table 1) in the horizontal x - y plane at the hub height. The wind turbine array is in full-wake configuration $\alpha = 0°$ in Cases (a-c) and partial-wake configuration $\alpha = 3°$ in Cases (d-f).

doi:10.20944/preprints202301.0417.v1

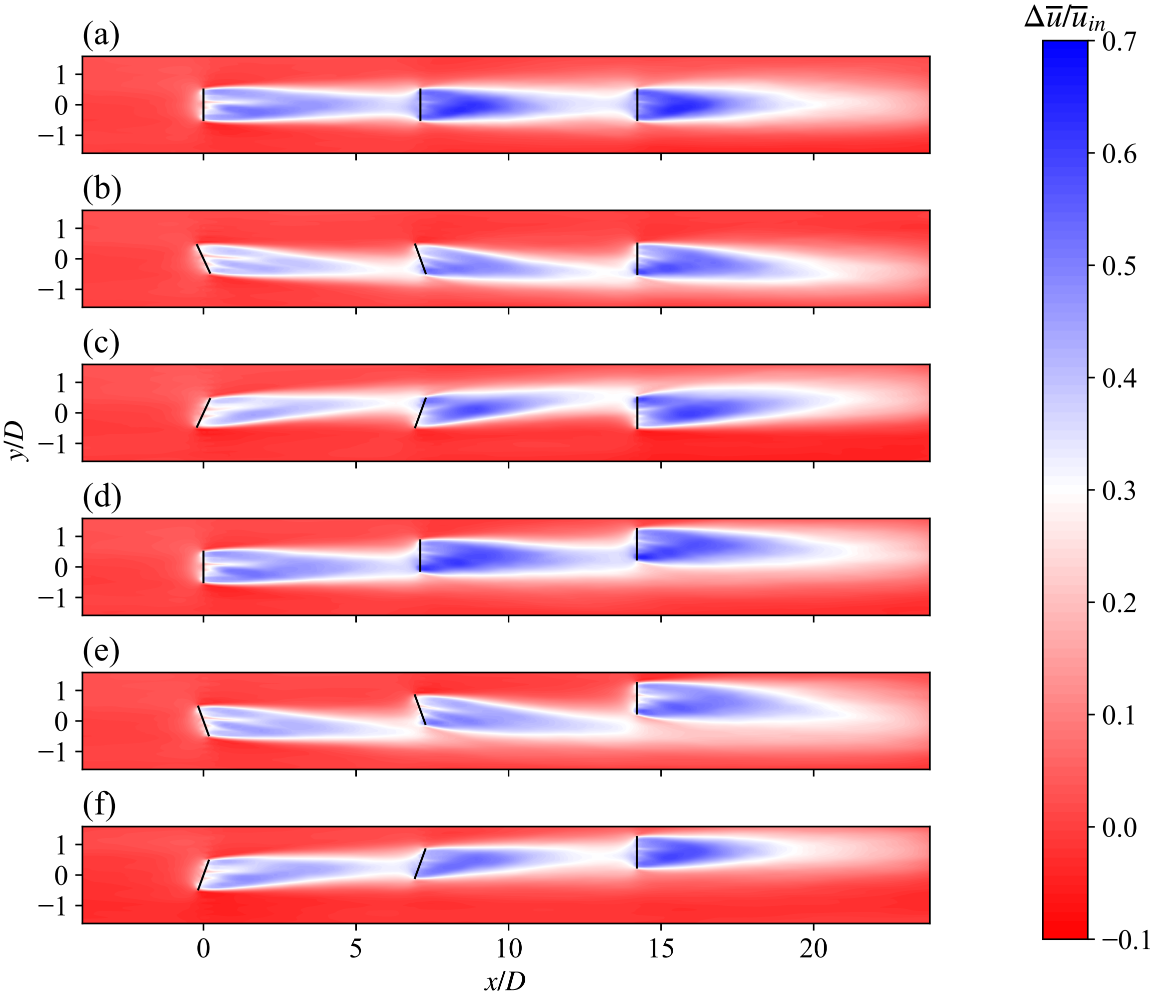

Figure 4. Top-view x - y cross-section contours of normalised streamwise mean velocity deficits $\Delta\overline{u}/\overline{u}_{in}$ at the hub height. Full-wake configuration ($\alpha = 0°$): (**a**) $\gamma = (0°, 0°, 0°)$; (**b**) $\gamma = (25°, 20°, 0°)$; (**c**) $\gamma = (-25°, -20°, 0°)$. Partial-wake configuration ($\alpha = 3°$): (**d**) $\gamma = (0°, 0°, 0°)$; (**e**) $\gamma = (25°, 20°, 0°)$; (**f**) $\gamma = (-25°, -20°, 0°)$.

Table 1. Configurations of six representative cases in full-wake and partial-wake configurations.

Case	Yaw angle (γ)	Inflow angle (α)
(a)	$(0°, 0°, 0°)$	0°
(b)	$(25°, 20°, 0°)$	0°
(c)	$(-25°, -20°, 0°)$	0°
(d)	$(0°, 0°, 0°)$	3°
(e)	$(25°, 20°, 0°)$	3°
(f)	$(-25°, -20°, 0°)$	3°

When the turbine array is in full-wake configuration $\alpha = 0°$ (Figures 4a - 4c), we observe that applying positive and negative yaw strategies deflects the wakes of upwind turbines away from downwind turbines. However, when the array is in partial-wake configuration $\alpha = 3°$ (Figures 4d - 4f), the positive yaw strategy is clearly more favourable due to the spanwise offset of the turbines: in Figure 4e, wake interference is largely avoided by applying positive yaw, whereas in Figure 4f, the application of negative yaw aggravates the interference of the wakes. We also observe the phenomenon of secondary wake deflection in the results, i.e., the additional deflection in the wake of a non-yawed turbine exposed to the wake of the yawed upwind turbine. For example, as shown in Figures 4b and

4c, although WT 3 itself is not yawed, the wake of WT 3 is still deflected when the turbine is exposed to the wake of the yawed upwind turbine. The secondary wake deflection is caused by the non-zero cross-flow in the wake of the yawed upwind turbine [31,32].

To further compare the wake structure of non-yawed and yawed turbines, in Figure 5 we show the contours of normalised mean streamwise velocity deficits $\Delta\overline{u}/\overline{u}_{in}$ in the vertical y - z cross-section plane 6D downwind of WT 1. The velocity deficit contours are overlapped with the vector fields of in-plane velocity components ($\overline{v}$ and $\overline{w}$). In the non-yawed case (Figure 5a), the velocity deficit region is largely circular; in the yawed cases (Figures 5b and 5c), a distinctive asymmetric kidney-shaped (curled) velocity deficit region is found in the wakes behind yawed turbines, which is associated with the formation of a counter-rotating vortex pair (CVP) [31–33]. The CVP is induced by the cross-flow in the wake, which creates a skewed inflow for downwind turbines and leads to additional wake deflection behind those turbines.

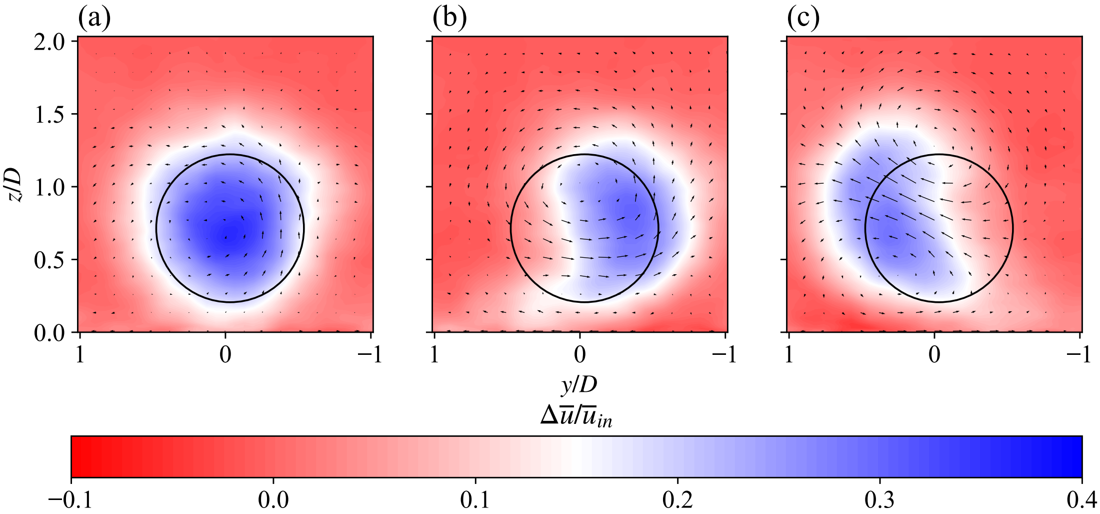

Figure 5. Front-view y - z cross-section contours of normalised streamwise velocity deficits $\Delta\overline{u}/\overline{u}_{in}$ at the location 6D downwind of WT 1, overlapped with vector fields of in-plane velocity components: (**a**) $\gamma_1 = 0°$; (**b**) $\gamma_1 = 25°$; (**c**) $\gamma_1 = -25°$.

Furthermore, as shown in Figure 5, the wake structure of the positively yawed turbine (Figure 5b) differs from its negatively yawed counterpart (Figure 5c). On the vertical y - z cross-section plane, the upper half of the velocity deficit region behind the positively yawed turbine is deflected further away from the domain centre-line ($y/D = 0$) than its counterpart behind the negatively yawed turbine. The lower half of the wake region, on the other hand, is closer to the centre line ($y/D = 0$) behind the positively yawed turbine than that of the negatively yawed one. The cross-flow in the wake of the positively yawed turbine is largely horizontal, whereas the direction of the cross-flow behind the negatively yawed turbine is around 45° upwards. Zong and Porté-Agel [32] observed a similar dichotomy of the wake structure of a positively and negatively yawed turbine in the wind tunnel experiments carried out in their study, and they explained it by the different vorticity evolution behind a positively yawed and negatively yawed turbine, which affects the deformation of the velocity deficit region.

3.2. Power production

The power production of wind farms subjected to AYC is an important metric for evaluating different AYC strategies. Figure 6 shows the normalised power outputs of the six representative cases specified in Table 1. In the full-wake configuration (Figure 6a), the positive and negative yaw strategies yield very similar power outputs for WTs 1 and 2; for WT 3, the negative yaw strategy yields 5.7% more power than the positive one due to the fact that negative yaw induces larger wake deflection than positive yaw [32]. In partial-wake configuration $\alpha = 3°$(Figure 6b), applying positive yaw achieves

doi:10.20944/preprints202301.0417.v1

power gains in the downwind turbines, while negative yaw redirects the wakes back to downwind turbines, as shown in Figure 5f, and leads to power losses for all three turbines.

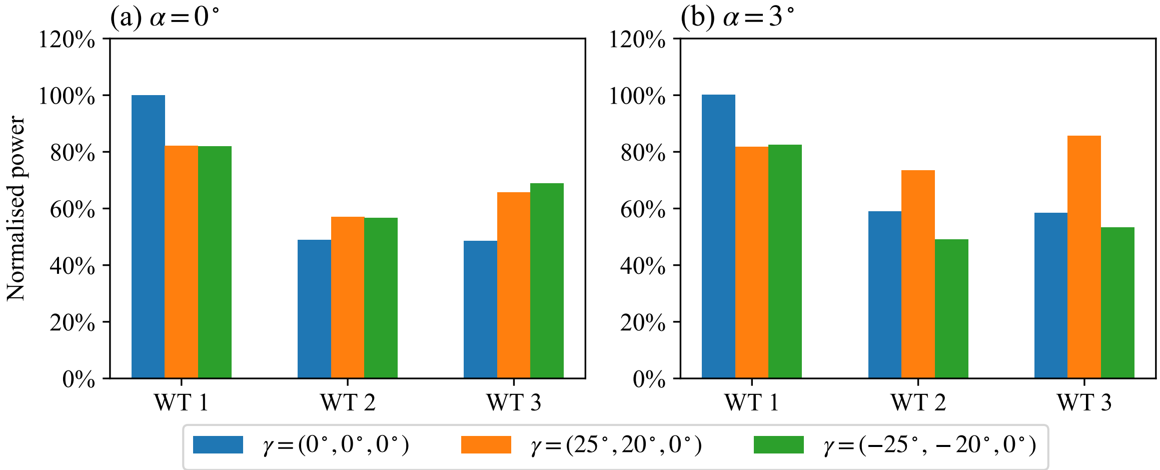

Figure 6. Normalised power outputs of different AYC configurations, normalised by the power of WT 1 in zero yaw (**a**) in full-wake configuration $\alpha = 0^\circ$ (**b**) in partial-wake configuration $\alpha = 3^\circ$.

Figure 7 shows the contours of the normalised total power gains in the AYC decision space $\boldsymbol{\Gamma}$ with different inflow angles α. The normalisation is done using the total power of the non-yawed baseline case P_0. The most noticeable difference between full-wake ($\alpha = 0^\circ$) and partial-wake ($\alpha \neq 0^\circ$) configurations is that there are two local optima in the decision space of the full-wake configuration, while only one optimum for partial-wake configurations. Consistent with the experimental results of Zong and Porté-Agel [5], the local power optimum corresponding to negative yaw (+5.14%) is larger than the one corresponding to positive yaw (+4.23%). Furthermore, in the partial-wake configurations under consideration ($\alpha = \pm 3^\circ,\ \pm 5^\circ$), smaller yaw angles are needed to alleviate the wake interference in the turbine array due to the spanwise offset of the wind turbines, and the power gains achieved by applying the optimal AYC are larger than the one in the full-wake configuration. The optimal power gains in the configurations with $\alpha = \pm 5^\circ$ are also smaller than their counterparts with $\alpha = \pm 3^\circ$. This observation can be explained by the fact that the turbines in the non-yawed baseline cases become less exposed to the wake flows with the increasing magnitude of the inflow angle; hence, the room for power improvement with AYC is reduced.

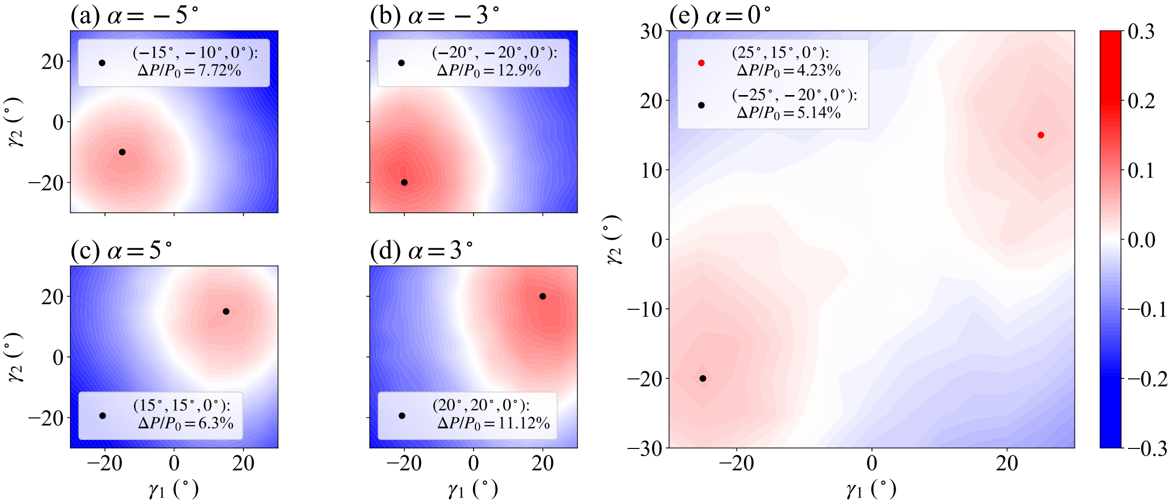

Figure 7. Normalised power gain contours in the AYC decision space $\boldsymbol{\Gamma}$ for different inflow angles. Black dots show the AYC configurations with the largest power gains.

3.3. Blade fatigue loading

Besides power production, fatigue loading is another critical metric to consider when applying AYC to a wind farm. Figure 8 shows the time-series segments of the flapwise bending moment (FBM) (Figure 8a) and the edgewise bending moment (EBM) (Figure 8b) at the blade root of WT 1. We find that, when the turbine is yawed, whether positively or negatively, the means of the FBM are decreased. However, a positively yawed turbine has a larger FBM variation than the non-yawed baseline, while a negatively yawed turbine has a smaller variation. As for the EBM, the differences between yawed and non-yawed turbines are less significant than the FBM because the variation in the EBM is dominated by the cyclic gravity load acting on rotating blades; thus, it is less sensitive to changes in the aerodynamic loads caused by AYC.

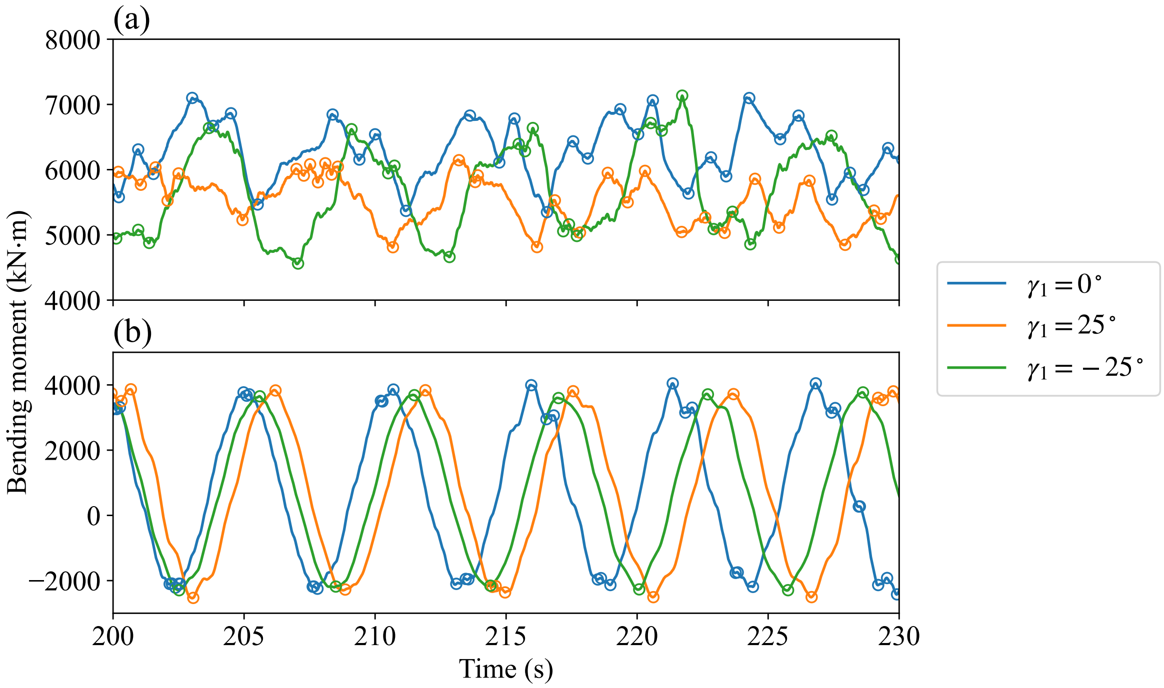

Figure 8. Time series segments of blade-root bending moments of WT 1: (**a**) flapwise bending moment; (**b**) edgewise bending moment. Empty cycles show the load reversal points extracted by the rainflow counting algorithm.

Using the transient blade loads extracted from the simulations, we further evaluate blade fatigue with the methodology discussed in Section 2.3. Figure 9 shows the flapwise and edgewise DELs for the wind turbine array at different AYC configurations. In full-wake configuration $\alpha = 0^\circ$, we observe that:

- In the flapwise direction (Figure 9a), the positive yaw case has larger DELs in WTs 1 and 2 and a slightly lower DEL in WT 3 compared to the non-yawed baseline. On the other hand, the negative yaw case has larger DELs in all three turbines.
- In the edgewise direction (Figure 9b), applying positive yaw slightly decreases the DEL in WT 1 while increasing it in WTs 2 and 3. The negative yaw strategy slightly decreases the DELs in all three turbines.

In partial-wake configuration $\alpha = 3^\circ$, we observe that:

- In the flapwise direction (Figure 9c), the DELs of WTs 2 and 3 are larger than those of WT 1 in the non-yawed baseline. This is because downwind turbines are partially exposed to the wakes of upwind turbines in this configuration, which creates significant load variations on the blades.

When the positive yaw strategy is adopted, as noted in the wake contour (Figure 4e), wake interference is largely avoided, and turbine fatigue loads are alleviated. Applying negative yaw in this configuration redirects the wakes to the downwind turbines (Figure 4f), alleviating partial wake overlapping. As a result, we observe decreases in the DELs of WT 2 and WT 3.

- In the edgewise direction (Figure 9d), applying positive yaw slightly decreases the DEL in WTs 1 and 2 while increasing it in WT 3. The negative yaw strategy slightly decreases the DELs in all three turbines. Similar to the full-wake configuration, the edgewise DELs are less sensitive to changes in yaw angles than the FBM.

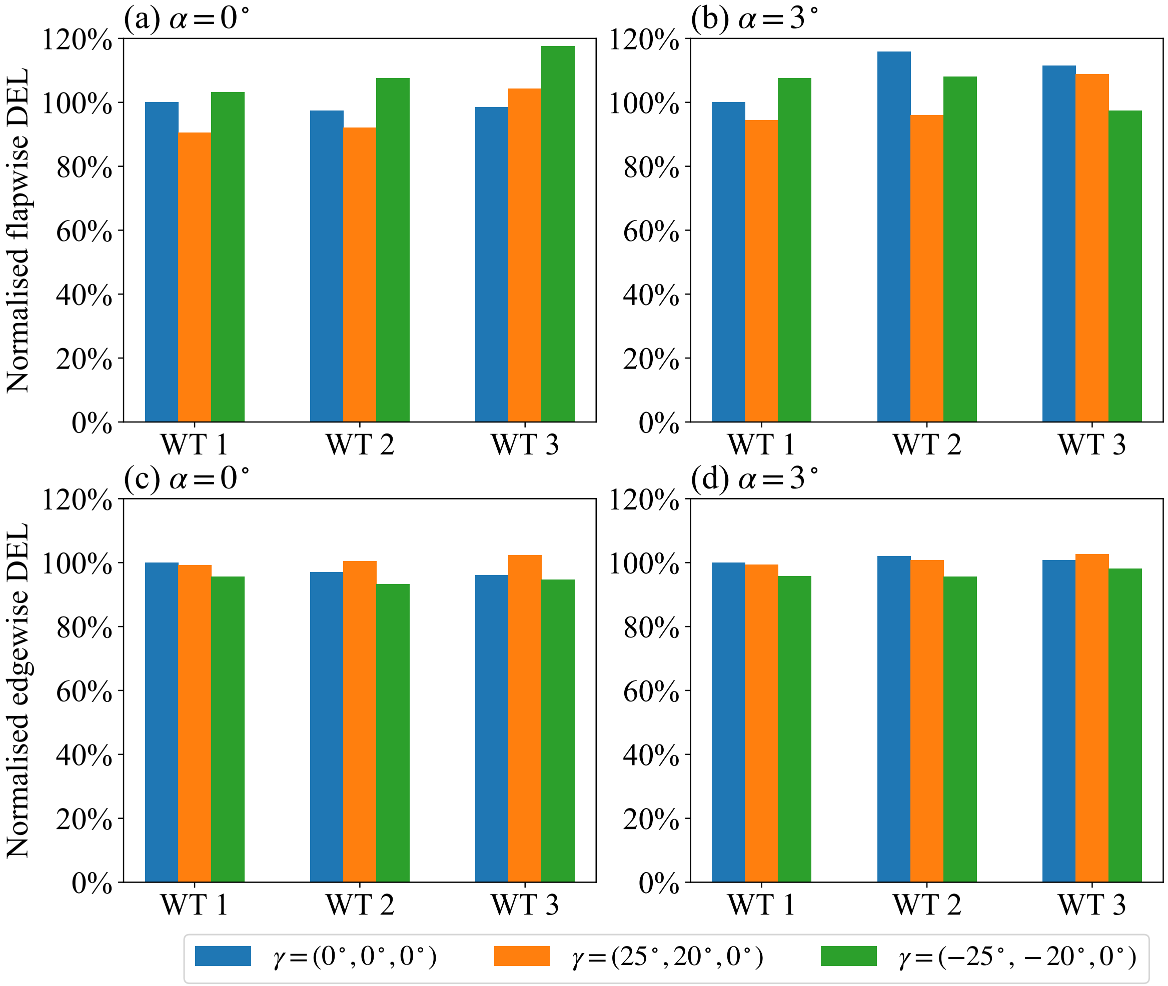

Figure 9. Normalised DELs of blade-root blending moments in different AYC configurations and inflow angles, normalised by the DELs of WT 1 in zero yaw condition: (**a**)-(**b**) flapwise bending moment; (**c**)-(**d**) edgewise bending moment.

To further reveal the relation between blade fatigue in the turbine array and AYC, we define the summation of the DEL of each turbine as the total DEL of the turbine array and compute the normalised total DEL variation $\Delta DEL/DEL_0$. The normalisation is done using the total DEL of the non-yawed baseline case DEL_0. Figure 10 shows the contours of $\Delta DEL/DEL_0$ in the flapwise (Figure 10a to 10e) and edgewise directions (Figure 10f to 10j) in the decision space $\mathbf{\Gamma}$ for different inflow angles. Consistent with our observations in Figures 8 and 9, we find that the changes in the flapwise DELs are more significant than in the edgewise DELs. Furthermore, in contrast to the power gain contours (Figure 7), we observe an asymmetry in the DEL variation contour: the AYC strategies with opposite signs for yaw and inflow angles produce similar power outputs but very different DELs. For example (Table 2), the two AYC strategies $\gamma = (-20^\circ, -20^\circ, 0^\circ)$, $\alpha = -3^\circ$ and $\gamma = (20^\circ, 20^\circ, 0^\circ)$, $\alpha = 3^\circ$ in the

doi:10.20944/preprints202301.0417.v1

decision space $\boldsymbol{\Gamma}$ yield similar power gains (12.9% vs 11.12%). However, the negative strategy increases the flapwise DEL ($+7.09\%$) and edgewise DEL ($+0.54\%$) from the non-yaw benchmark, while the positive strategy γ_+ decrease the flapwise DEL (-3.18%) but increases the edgewise DEL ($+0.99\%$).

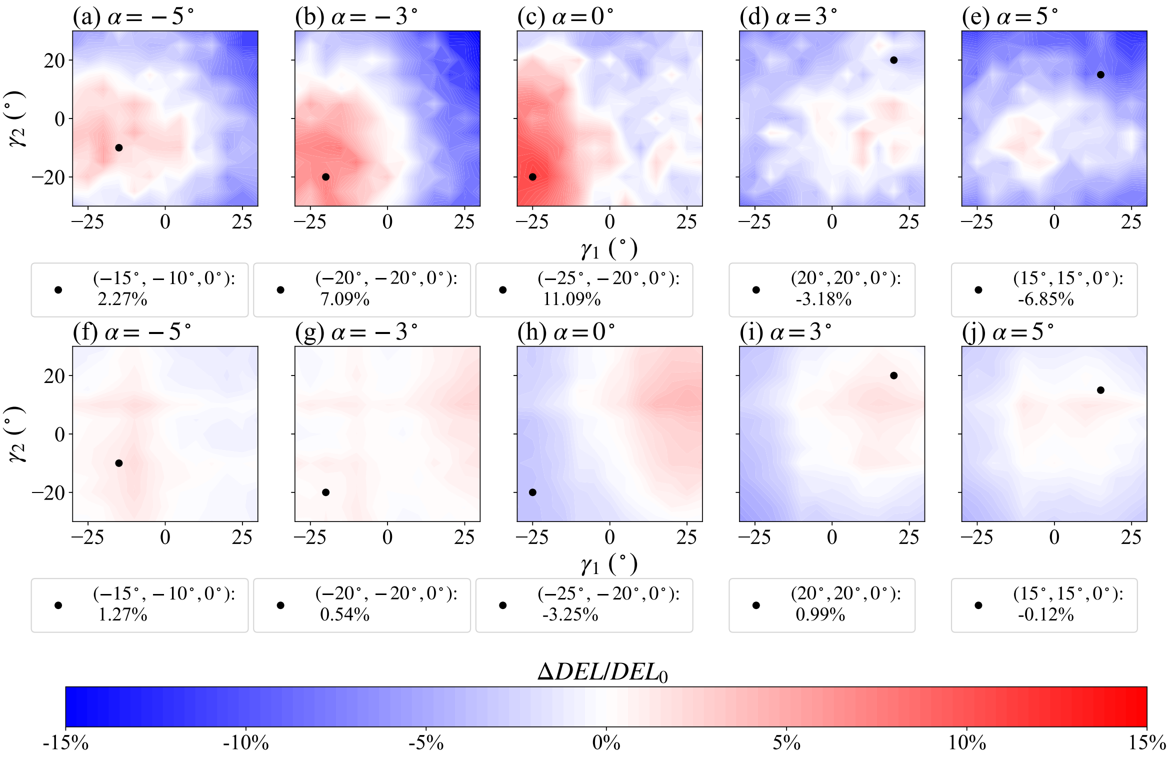

Figure 10. Normalised DEL variation contours in the AYC decision space $\boldsymbol{\Gamma}$ for different inflow angles for (**a**)-(**e**) flapwise bending moment; (**f**)-(**j**) edgewise bending moment. Black dots show the power-optimal AYC configurations and their corresponding DEL variations.

Table 2. Power gains and DEL variations for the configurations with opposite yaw and inflow angles.

Yaw angles (γ)	Inflow angle (α)	$\Delta P/P_0$	$\Delta DEL_F/DEL_{F,0}$	$\Delta DEL_E/DEL_{E,0}$
$(-20°, -20°, 0°)$	$-3°$	12.9 %	7.09%	0.54%
$(20°, 20°, 0°)$	$3°$	11.12%	-3.18%	0.99%

4. Theoretical analysis on flapwise blade fatigue in positive and negative yaw strategies

Figures 9 and 10 have shown that applying positive or negative yaw strategies leads to significantly different flapwise fatigue loading not only in the yawed turbines but also in the non-yawed turbines exposed to the wakes of yawed upwind turbines. In this section, we present a theoretical analysis of the causes of these differences.

Flapwise blade fatigue is induced by the variations of the force normal to the rotor disk F_n (Figure 11) acting on wind turbine blades. The force variation can be attributed to inflow turbulence and blade rotation. For a front-row turbine, it experiences the same level of inflow turbulence when it is positively or negatively yawed with the same yaw magnitude. Therefore, the difference in flapwise fatigue is mostly caused by the different blade-force variations per rotation, which can be analysed by the blade element momentum (BEM) theory. Computing the aerodynamic forces acting on the rotating wind turbine blades based on the BEM theory requires an iterative process. However, we can simplify this process into closed-form expressions with reasonable approximations and directly analyse the variation of aerodynamic loads.

According to the velocity and force triangles in the BEM theory shown in Figure 11, the normal force F_n acting on a blade element per unit length can be expressed as:

$$F_n = \frac{1}{2} c \rho V_{rel}^2 C_n, \tag{7}$$

$$V_{rel} = \frac{V_t}{\cos\varphi}, \tag{8}$$

$$C_n = C_L \cos\varphi + C_d \sin\varphi, \tag{9}$$

$$\tan\varphi = \frac{V_n}{V_t}, \tag{10}$$

where c is the chord length, ρ is the air density, V_{rel} is the magnitude of the resultant local relative velocity of the rotating blade with respect to the flow, V_t and V_n are the magnitudes of V_{rel}, respectively, and φ is the angle between resultant relative velocity and the rotation plane.

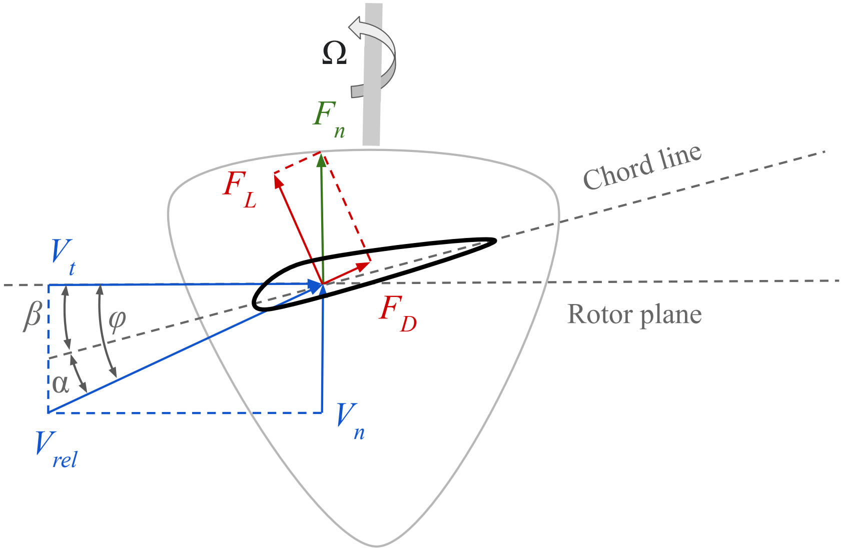

Figure 11. Schematic plot of the velocity and force triangles on a rotating wind turbine blade based on the BEM theory.

We approximate F_n by substituting Eqs. 8 - 10 into Eq. 7 and apply small-angle approximations to the trigonometric functions of φ:

$$F_n \approx \frac{1}{2} c \rho V_t^2 (C_L + C_d \varphi). \tag{11}$$

The approximations of the trigonometric functions can be justified by the fact that the FBM at the blade root is dominated by the flapwise loads acting on the sections near the blade tip. In those sections, the flow angle φ, angle of attack (AoA) α, and blade twist angle β are small.

According to classical thin airfoil theory [34] and the fact that the twist angle β is small, the lift coefficient C_L of an airfoil in small AoAs can be approximated by:

$$C_L \approx 2\pi\alpha, \tag{12}$$

$$\alpha = \varphi - \beta \approx \varphi. \tag{13}$$

Substituting Eqs. 12 and 13 into Eq. 11, we have:

$$F_n \approx \frac{1}{2} c \rho V_t^2 (2\pi + C_d)\varphi. \tag{14}$$

Considering the fact that $C_d \ll 2\pi$ at small AoAs, we neglect the contribution of C_d and further simplify Eq. 14 to:

$$F_n \approx \pi c \rho V_t V_n. \tag{15}$$

We find that F_n is approximately proportional to the product of V_t and V_n:

$$F_n \propto V_t V_n. \tag{16}$$

Therefore, to study the variation of the normal force F_n, we can focus on the variation of $V_t V_n$. Since the tangential induction is very weak in the blade sections close to the tip, we neglect the contribution of tangential induction and derive V_t and V_n of a yawed turbine according to the BEM theory [35]:

$$V_n = V_0(\cos\gamma - a), \tag{17}$$

$$V_t = \Omega r + V_0 \cos\psi (a \tan\frac{\chi}{2} - \sin\gamma), \tag{18}$$

where V_0 is the freestream inflow velocity to the turbine, γ is the turbine yaw angle, Ω is the turbine rotation speed, r is the distance of the blade element to the hub, ψ is the phase angle of the rotating blade, χ is the wake skewing angle, and a is the axial induction factor of the turbine. Glauert [36] proposed that the axial induction factor a can be approximated by:

$$a = a_0(1 + f(\frac{r}{R})K(\chi)\sin\psi), \tag{19}$$

where a_0 is the induction factor of the turbine in non-yawed condition, R is the radius of the turbine, and f is the wake expansion function. Øye [37] proposed the following polynomial fit for f:

$$f(\frac{r}{R}) = \frac{1}{2}(\frac{r}{R} + 0.4(\frac{r}{R})^3 + 0.4(\frac{r}{R})^5). \tag{20}$$

Coleman [38] proposed that $K(\chi)$ can be approximated by:

$$K(\chi) = 2\tan(\frac{\chi}{2}),\ \chi = (0.6a_0 + 1)\gamma. \tag{21}$$

As an example, we consider the $V_n V_t$ variations in a front-row turbine with $\gamma_1 = \pm 25^\circ$ at the blade location $r = 0.7R$ in a uniform inflow and a vertically sheared inflow. The non-yawed induction factor is assumed to be azimuthally unchanged and take the theoretical optimal value predicted by the BEM theory:

$$a_0 = 1/3. \tag{22}$$

Figure 12 shows the freestream inflow velocity V_0 to the blade section $r = 0.7R$ at different heights z and different blade phase angles ψ. We can see that V_0 varies with ψ in the vertically sheared flow while staying constant in the uniform inflow. When the turbine rotates in the vertically sheared inflow, the azimuthal distributions of the local relative velocity on blade sections in the positively and negatively yawed turbine are different. Figure 13 shows the variation of $V_t V_n$ computed from Eq. 17 and 18 with respect to ψ in the two different inflows shown in Figure 13. We find that the magnitudes of the variation for the positive and negative yaw angles are the same in the uniform inflow. However, in the vertically sheared inflow, the negative yaw angle leads to a larger variation of $V_t V_n$ than the positive yaw angle. As a result, according to Eq. 16, the negatively yawed turbine endures larger variation of the normal thrust force per rotation and, consequently, greater flapwise blade fatigue than the positively yawed one.

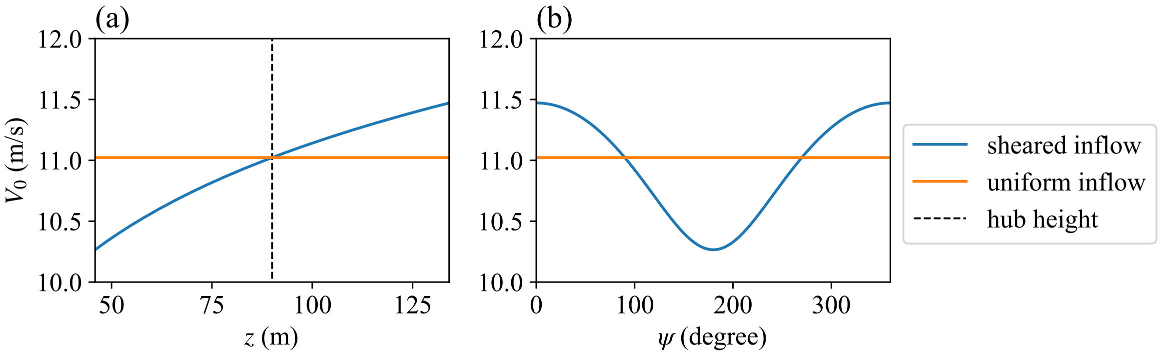

Figure 12. Freestream inflow velocity to the turbine blade section $r = 0.7R$: (**a**) at different vertical heights; (**b**) at different blade phase angles.

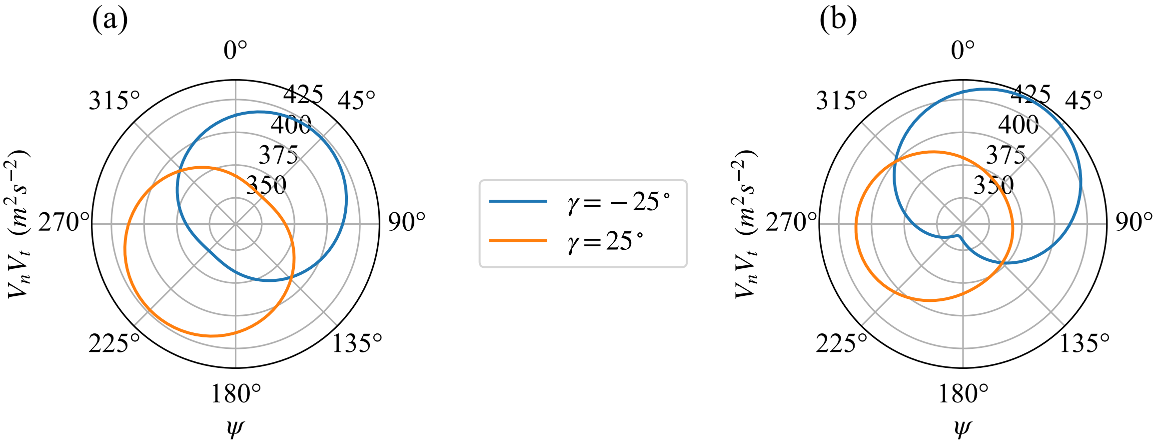

Figure 13. Azimuthal variations of $V_n V_t$ at $r = 0.7R$ with respect to the blade phase angle ψ predicted by the BEM theory in (**a**) a uniform inflow $u(z) = 11$ m/s; (**b**) a vertically sheared inflow $u(z) = \frac{u_*}{\kappa}\log(z/z_0)$, in which $u_* = 0.45$ m/s, $\kappa = 0.4$, and $z_0 = 0.005$ m.

Furthermore, applying positive or negative yaw to the upwind turbine also affects the flapwise blade fatigue in its downwind turbine, even if the downwind turbine is not yawed, due to the different wake structures between the positively and negatively yawed turbine. For example, for a non-yawed turbine installed 7D downstream of WT 1 without spanwise offset, the front-view contours of its inflow statistics (normalised mean velocity and turbulence intensity) 1D in front of the downwind turbine are shown in Figure 14. The spanwise deflection of the wake of the negatively yawed WT 1 is larger than that of the positively yawed WT 1. As a result, the azimuthal variation of the streamwise inflow velocity for the downwind turbine in the wake of the negatively yawed WT 1 is larger than that in the wake of the negatively yawed WT 1. The turbine in the wake of the negatively yawed WT 1 is also exposed to a higher level of streamwise turbulence than that in the wake of the positively yawed WT 1. Therefore, in this configuration, the downwind turbine would endure higher flapwise blade fatigue if it is in the wake of a negatively yawed turbine than that of a positively yawed turbine. The simulation results confirm that the flapwise DEL of the non-yawed WT 2 in the AYC case $\gamma = (-25^\circ, 0^\circ, 0^\circ)$, $\alpha = 0^\circ$ is 7.7% higher than its counterpart in the AYC case $\gamma = (25^\circ, 0^\circ, 0^\circ)$, $\alpha = 0^\circ$.

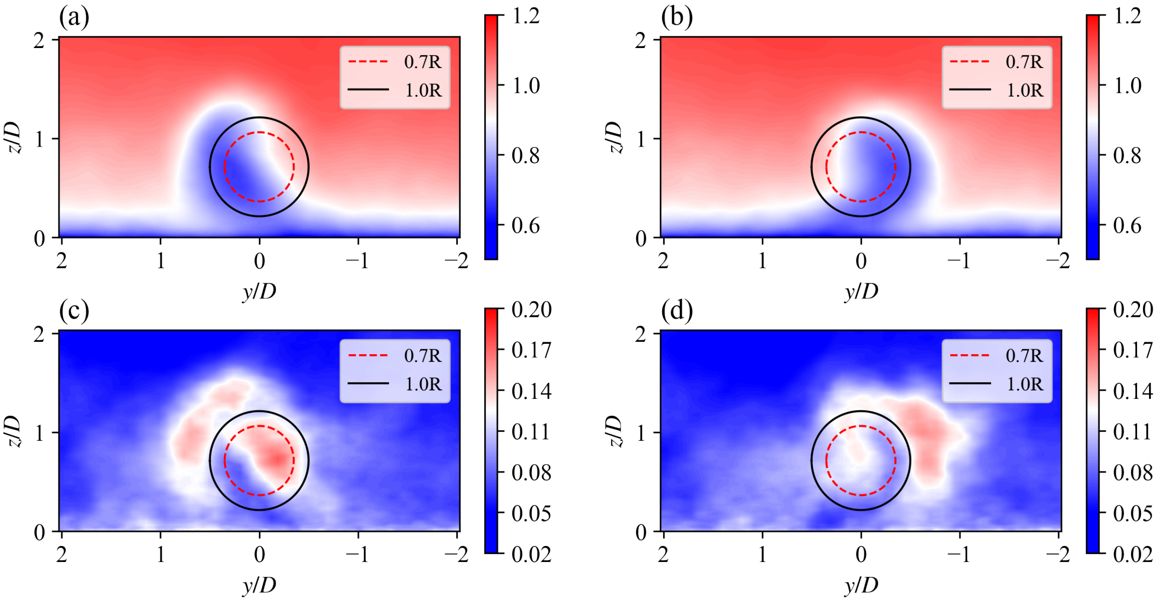

Figure 14. Front-view y - z cross-section contours of normalised streamwise mean velocity and turbulence intensity I_u at the location 6D downwind of WT 1: (**a**) $\overline{u}/\overline{u}_{in}$, $\gamma_1 = -25°$; (**b**) $\overline{u}/\overline{u}_{in}$, $\gamma_1 = 25°$; (**c**) I_u, $\gamma_1 = -25°$; (**d**) I_u, $\gamma_1 = 25°$. Black and red circles represent the trajectories of the blade sections $r = 1.0R$ and $r = 0.7R$ of the rotating blade, respectively.

5. Discussion and conclusions

In this study, we investigate the power production and blade fatigue of a three-turbine array in full-wake and partial-wake configurations using a two-way coupled aeroelastic-LES framework. The simulations are carried out at discrete decision points of the AYC decision space $\mathbf{\Gamma}$ spanned by the yaw angles of the first two turbines: $\mathbf{\Gamma} = \{\gamma_1 : -30°, -25°, ..., 25°, 30°\} \times \{\gamma_2 : -30°, -25°, ..., 25°, 30°\}$. We extract the time series of the power and the blade bending moments from the simulations and compute the mean power outputs and the blade fatigue loads of the turbine array.

In full-wake configuration $\alpha = 0°$, we observe two local power optima in the explored AYC decision space $\mathbf{\Gamma}$: one in the positive quadrant ($\gamma_1 > 0°, \gamma_2 > 0°$) and another one in the negative quadrant ($\gamma_1 < 0°, \gamma_2 < 0°$). The optimal yaw strategy with positive yaw angles yields slightly less power than that with negative yaw angles. We also find that the locally power-optimal positive yaw strategy endures less flapwise blade fatigue and more edgewise blade fatigue than its counterpart with negative yaw angles.

In partial-wake configurations $|\alpha| = 3°$ and $5°$, there is only one power optimum in the explored decision space. Due to the spanwise offset of the turbines, applying optimal AYC achieves larger optimal power gains than that in the full-wake configuration. When the magnitude of α increases from $|\alpha| = 3°$ to $5°$, the optimal power gains start to decrease, as the non-yawed baseline in this configuration is less affected by wake interference. As for the blade fatigue, when the inflow angle α is positive, applying the power-optimal yaw strategy in the positive quadrant of the AYC decision space achieves power gains while reducing the flapwise blade fatigue. In contrast, when the inflow angle is negative, the power-optimal strategies with negative inflow angles lead to higher flapwise blade fatigue than the baseline case. Compared with the flapwise fatigue, the variations of the edgewise fatigue loading to different AYC strategies are less significant in the partial-wake configurations under consideration.

Furthermore, through a BEM-based analysis, we reveal that, for the front-row turbine, the aforementioned differences in the flapwise blade fatigue between the positively and negatively yawed turbine are caused by the different azimuthal variations of the local relative velocity on blade sections, which result from the combined effects of vertical wind shear and blade rotation. For the downwind turbine exposed to the wake of the yawed turbine, the differences in the flapwise blade fatigue are caused by the different wake deficit and turbulence distributions in the wake of the positively and negatively yawed turbine. These findings highlight that, in the wake modelling of wind turbines subjected to AYC, it is necessary to consider the inflow inhomogeneity and blade rotation, as well as the differences between the wake structures of positively and negatively yawed turbines, particularly when fatigue evaluation is needed from the model.

Author Contributions: Conceptualization, Mou Lin and Fernando Porté-Agel; Data curation, Mou Lin and Fernando Porté-Agel; Formal analysis, Mou Lin and Fernando Porté-Agel; Funding acquisition, Fernando Porté-Agel; Investigation, Mou Lin and Fernando Porté-Agel; Methodology, Mou Lin and Fernando Porté-Agel; Project administration, Fernando Porté-Agel; Resources, Fernando Porté-Agel; Software, Mou Lin; Supervision, Fernando Porté-Agel; Validation, Mou Lin and Fernando Porté-Agel; Visualization, Mou Lin; Writing—original draft, Mou Lin; Writing—review & editing, Mou Lin and Fernando Porté-Agel.

Funding: This research was funded by the Swiss Federal Office of Energy (Grant SI/501337-01) and the Swiss National Science Foundation (Grants 200021_172538). In addition, this project was carried out within the frame of the Swiss Centre for Competence in Energy Research on the Future Swiss Electrical Infrastructure (SCCER-FURIES) with the financial support of the Swiss Innovation Agency (Innosuisse - SCCER program, contract number: 1155002544).

Data Availability Statement: The dataset is available upon request.

Acknowledgments: The authors would like to thank Álex Socías Villanueva for his contribution in the code development.

Conflicts of Interest: The authors declare no conflict of interest.

Abbreviations

The following abbreviations are used in this manuscript:

ABL	Atmospheric boundary layer
ALM	Actuator line model
AoA	Angle of attack
AYC	Active yaw control
BEM	Blade element momemtum
CVP	Counter-rotating vortex pair
DEL	Damage equivalent load
EALM	Elastic actuator line model
EBM	Edgewise bending moment
FBM	Flapwise bending moment
LES	Large-eddy simulation
WT	Wind turbine

References

1. Grant, I.; Parkin, P.; Wang, X. Optical vortex tracking studies of a horizontal axis wind turbine in yaw using laser-sheet, flow visualisation. *Exp. Fluids* **1997**, *23(6)*, 513. doi:10.1007/s003480050142.
2. Medici, D.; Alfredsson, P. Measurements on a wind turbine wake: 3D effects and bluff body vortex shedding. *Wind Energy* **2006**, *9*, 219–236. doi:https://10.1002/we.156.
3. Howland, M.F.; Bossuyt, J.; Martínez-Tossas, L.A.; Meyers, J.; Meneveau, C. Wake structure in actuator disk models of wind turbines in yaw under uniform inflow conditions. *J. Renew. Sustain Ener.* **2016**, *8*, 043301. doi:10.1063/1.4955091.
4. Bastankhah, M.; Porté-Agel, F. Wind farm power optimization via yaw angle control: A wind tunnel study. *J. of Renew. Sustain. Ener.* **2019**, *11*, 023301. doi:10.1063/1.5077038.
5. Zong, H.; Porté-Agel, F. A momentum-conserving wake superposition method for wind farm power prediction. *Renew. Energ.* **2021**, *170*, 1228. doi:10.1017/jfm.2020.77.
6. Campagnolo, F.; Castellani, F.; Natili, F.; Astolfi, D.; Mühle, F. Wind Tunnel Testing of Yaw by Individual Pitch Control Applied to Wake Steering. *Front. Energy Res.* **2022**, *10*. doi:10.3389/fenrg.2022.883889.

doi:10.20944/preprints202301.0417.v1

7. Jiménez, A.; Crespo, A.; Migoya, E. Application of a LES technique to characterize the wake deflection of a wind turbine in yaw. *Wind Energy* **2010**, *13*, 559–572. doi:10.1002/we.380.
8. Fleming, P.A.; Gebraad, P.M.; Lee, S.; van Wingerden, J.W.; Johnson, K.; Churchfield, M.; Michalakes, J.; Spalart, P.; Moriarty, P. Evaluating techniques for redirecting turbine wakes using SOWFA. *Renew. Energ.* **2014**, *70*, 211–218.
9. Munters, W.; Meyers, J. Dynamic strategies for yaw and induction control of wind farms based on large-eddy simulation and optimization. *Energies* **2018**, *11(1)*, 177. doi:10.3390/en11010177.
10. Fleming, P.; Annoni, J.; Churchfield, M.; Martinez-Tossas, L.A.; Gruchalla, K.; Lawson, M.; Moriarty, P. A simulation study demonstrating the importance of large-scale trailing vortices in wake steering. *Wind Energy Sci.* **2018**, *3*, 243–255. doi:10.5194/wes-3-243-2018.
11. Archer, C.L.; Vasel-Be-Hagh, A. Wake steering via yaw control in multi-turbine wind farms: Recommendations based on large-eddy simulation. *Sustain. Energy Tech. and Assess.* **2019**, *33*, 34. doi:10.1016/j.seta.2019.03.002.
12. Lin, M.; Porté-Agel, F. Large-eddy simulation of yawed wind-turbine wakes: comparisons with wind tunnel measurements and analytical wake models. *Energies* **2019**, *12*, 4574. doi:10.3390/en12234574.
13. Kragh, K.A.; Hansen, M.H. Load alleviation of wind turbines by yaw misalignment. *Wind Energy* **2014**, *17*, 971–982. doi:doi.org/10.1002/we.1612.
14. Zalkind, D.S.; Pao, L.Y. The fatigue loading effects of yaw control for wind plants. 2016 American Control Conference (ACC). IEEE, 2016, pp. 537–542.
15. Fleming, P.; Gebraad, P.M.; Lee, S.; van Wingerden, J.W.; Johnson, K.; Churchfield, M.; Michalakes, J.; Spalart, P.; Moriarty, P. Simulation comparison of wake mitigation control strategies for a two-turbine case. *Wind Energy* **2015**, *18*, 2135–2143. doi:10.1002/we.1810.
16. Damiani, R.; Dana, S.; Annoni, J.; Fleming, P.; Roadman, J.; van Dam, J.; Dykes, K. Assessment of wind turbine component loads under yaw-offset conditions. *Wind Energy Sci.* **2018**, *3*, 173–189. doi:10.5194/wes-3-173-2018.
17. Gebraad, P.; Thomas, J.J.; Ning, A.; Fleming, P.; Dykes, K. Maximization of the annual energy production of wind power plants by optimization of layout and yaw-based wake control. *Wind Energy* **2017**, *20*, 97–107. doi:10.1002/we.1993.
18. van Dijk, M.T.; van Wingerden, J.; Ashuri, T.; Li, Y. Wind farm multi-objective wake redirection for optimizing power production and loads. *Energy* **2017**, *121*, 561–569.
19. Kanev, S.; Savenije, F.; Engels, W. Active wake control: An approach to optimize the lifetime operation of wind farms. *Wind Energy* **2018**, *21*, 488–501.
20. Reyes, H.M.; Kanev, S.; Doekemeijer, B.; van Wingerden, J.W. Validation of a lookup-table approach to modeling turbine fatigue loads in wind farms under active wake control. *Wind Energy Science* **2019**, *4*, 549–561. doi:10.5194/wes-4-549-2019.
21. Lin, M.; Porté-Agel, F. Power maximization and fatigue-load mitigation in a wind-turbine array by active yaw control: an LES study. Journal of Physics: Conference Series. IOP Publishing, 2020, Vol. 1618, p. 042036. doi:10.1088/1742-6596/1618/4/042036.
22. Wu, Y.T.; Porté-Agel, F. Large-eddy simulation of wind-turbine wakes: evaluation of turbine parametrisations. *Bound-lay. Meteorol.* **2011**, *138*, 345. doi:10.1007/s10546-010-9569-x.
23. Porté-Agel, F.; Wu, Y.T.; Lu, H.; Conzemius, R.J. Large-eddy simulation of atmospheric boundary layer flow through wind turbines and wind farms. *J. Wind Eng. Ind. Aerod.* **2011**, *99*, 154–168. doi:10.1016/j.jweia.2011.01.011.
24. Abkar, M.; Porté-Agel, F. Influence of atmospheric stability on wind-turbine wakes: A large-eddy simulation study. *Phys. Fluids* **2015**, *27*, 035104. doi:10.1063/1.4913695.
25. Meng, H.; Lien, F.S.; Li, L. Elastic actuator line modelling for wake-induced fatigue analysis of horizontal axis wind turbine blade. *Renewable energy* **2018**, *116*, 423–437. doi:10.1016/j.renene.2017.08.074.
26. Lu, H.; Porté-Agel, F. A modulated gradient model for large-eddy simulation: Application to a neutral atmospheric boundary layer. *Phys. Fluids* **2010**, *22*, 015109. doi:10.1063/1.3291073.
27. Sørensen, J.N.; Shen, W.Z. Numerical modeling of wind turbine wakes. *J. Fluids Eng.* **2002**, *124*, 393–399.
28. Jonkman, J.; Butterfield, S.; Musial, W.; Scott, G. Definition of a 5-MW reference wind turbine for offshore system development. Technical report, National Renewable Energy Lab.(NREL), Golden, CO (United States), 2009. doi:10.2172/947422.

29. Freebury, G.; Musial, W. Determining equivalent damage loading for full-scale wind turbine blade fatigue tests. 2000 ASME wind energy symposium, 2000, p. 50.
30. *IEC 61400-1:2019, Wind energy generation systems - Part 1: Design requirements*, 3. ed.; International Electrotechnical Commission, 2019.
31. Bastankhah, M.; Porté-Agel, F. Experimental and theoretical study of wind-turbine wakes in yawed conditions. *J. Fluid Mech.* **2016**, *806*, 506–541. doi:10.1017/jfm.2016.595.
32. Zong, H.; Porté-Agel, F. A point vortex transportation model for yawed wind turbine wakes. *J. Fluid Mech.* **2020**, *890*, A8. doi:10.1017/jfm.2020.123.
33. Shapiro, C.R.; Gayme, D.F.; Meneveau, C. Modelling yawed wind turbine wakes: a lifting line approach. *J. Fluid Mech.* **2018**, *841*, R1. doi:10.1017/jfm.2018.75.
34. Anderson, J. *Fundamentals of Aerodynamics*; McGraw Hill, 2011.
35. Burton, T.; Jenkins, N.; Sharpe, D.; Bossanyi, E. *Wind Energy Handbook*; John Wiley & Sons, 2011.
36. Glauert, H. The theory of the autogyro. *The Aeronautical Journal* **1927**, *31*, 483–508.
37. Øys, S. Induced velocity for rotors in yaw. Proceedings of the 6th IEA Symposium on the Aerodynamics of Wind Turbines. ECN, Petten, Neitherland, 1992.
38. Coleman, R.P.; Feingold, A.M.; Stempin, C.W. Evaluation of the induced-velocity field of an idealized helicoptor rotor. Technical report, National Aeronautics and Space Administration Hampton Va Langley Research Center, 1945.